

The novel asymmetric entry intermediate of a picornavirus captured with nanodiscs

Hyunwook Lee,^{1*} Kristin L. Shingler,^{1*} Lindsey J. Organtini,¹ Robert E. Ashley,¹ Alexander M. Makhov,² James F. Conway,² Susan Hafenstein^{1†}

2016 © The Authors, some rights reserved; exclusive licensee American Association for the Advancement of Science. Distributed under a Creative Commons Attribution NonCommercial License 4.0 (CC BY-NC). 10.1126/sciadv.1501929

Many nonenveloped viruses engage host receptors that initiate capsid conformational changes necessary for genome release. Structural studies on the mechanisms of picornavirus entry have relied on *in vitro* approaches of virus incubated at high temperatures or with excess receptor molecules to trigger the entry intermediate or A-particle. We have induced the coxsackievirus B3 entry intermediate by triggering the virus with full-length receptors embedded in lipid bilayer nanodiscs. These asymmetrically formed A-particles were reconstructed using cryo-electron microscopy and a direct electron detector. These first high-resolution structures of a picornavirus entry intermediate captured at a membrane with and without imposing icosahedral symmetry (3.9 and 7.8 Å, respectively) revealed a novel A-particle that is markedly different from the classical A-particles. The asymmetric receptor binding triggers minimal global capsid expansion but marked local conformational changes at the site of receptor interaction. In addition, viral proteins extrude from the capsid only at the site of extensive protein remodeling adjacent to the nanodisc. Thus, the binding of the receptor triggers formation of a unique site in preparation for genome release.

INTRODUCTION

The human pathogen coxsackievirus B3 (CVB3) causes myocarditis and pancreatitis and has been implicated in the development of type 1 diabetes mellitus (1–5). Like other picornaviruses, CVB3 has a small, 30-nm-diameter nonenveloped capsid composed of structural proteins VP1 to VP4. The simple icosahedral architecture, $T = 1$ (pseudo $T = 3$), displays 60 repeating asymmetric units with 60 potential receptor binding sites (6). Picornavirus entry is mediated by binding a specific receptor at the host cell membrane, which initiates endocytosis and, in many family members, triggers formation of the altered particle, or “A-particle,” that is a necessary entry intermediate (7, 8). For some picornaviruses, this receptor interaction occurs at a cleft surrounding each fivefold vertex, called the “canyon” (9). An opening in the canyon floor leads to a hydrophobic pocket that contains a lipid moiety called the “pocket factor,” which is absent in A-particle structures (10–13), suggesting a function during entry.

The final stages of entry have been studied by several low-resolution asymmetric structures formed on liposomes (14–17) and by higher-resolution icosahedrally averaged A-particles made by applying global capsid stimulation, such as heat or excess soluble receptor molecules (11, 13, 18–20). These and other structures suggest a model of entry whereby binding of receptor initiates conformational changes beginning with loss of pocket factor, followed by an irreversible capsid expansion (20). The internal VP1 N termini subsequently extrude through the capsid shell at the quasi-threefold axis, at a raised region termed the “propeller tip,” and embed into the endosome membrane, anchoring the A-particle by forming an amphipathic helix (11, 18, 21–23). VP4 then exits the capsid, and approximately 6 to 10 copies of this myristoylated viral protein form a pore in the membrane through which the RNA genome passes (22). To date, high-resolution A-particle

structures formed by excess external stimuli show these changes occurring throughout the capsid, in addition to openings that appear at the icosahedral twofold axes, which have been suggested as the RNA exit site (11–13). In addition, the transition to A-particle may be accompanied by an aberrant, partial loss of RNA (13, 18, 19); however, for poliovirus and CVB3, in an infection, RNA remains sequestered inside the A-particle for 30 to 90 min until a second unknown trigger initiates release into the cytoplasm of the host cell (24–26).

Despite previous work, much remains unknown about the entry of nonenveloped viruses. Because the virus binds to the host receptor in a focused or asymmetric interaction *in vivo*, high-resolution reconstructions of asymmetric structures are required to understand the mechanics of virus entry. A transformative advance in the field of cryo-electron microscopy (cryo-EM) now makes this possible. Direct electron detectors, such as the Falcon II camera used here, in combination with field emission gun microscopes and automated data collection software, result in atomic and near-atomic resolution structures of protein assemblies that are in a native, hydrated state (27–29). A recent improvement in image processing software is also supporting the advance in the field (30).

This study presenting CVB3 and its receptor, the coxsackie-adenovirus receptor (CAR), provides unprecedented insight into the virus entry intermediate formed by an interaction with the full-length receptor embedded in a lipid bilayer disc, or nanodisc, which better approximates a physiological interaction of virus and receptor than an application of heat or excess soluble proteins. Three-dimensional (3D) reconstructions with and without imposing icosahedral symmetry provide the first detailed structures that elucidate what virus components are required to change globally or asymmetrically for virus entry and release of the viral genome. Even for these highly mutable RNA viruses, the molecular entry mechanisms that have evolved may prove to be conserved and stable, intolerant of mutations, and, thus, good candidates for specific and targeted drug design.

¹The Pennsylvania State University College of Medicine, Hershey, PA 17033, USA. ²University of Pittsburgh School of Medicine, Pittsburgh, PA 15260, USA.

*These authors contributed equally to this work.

†Corresponding author. Email: shafenstein@hmc.psu.edu

RESULTS

Nanodiscs capture a virus entry complex

Attaining a high-resolution asymmetric structure of A-particle demands a new approach. Discrete lipid bilayer discs formed from lipids and scaffolding proteins have been used for analyses of membrane protein structure and function (31–33). Here, we exploit these nanodiscs to asymmetrically present the receptor protein to the infectious virus. Inserting CAR via the transmembrane domain into the nanodiscs creates a 12-nm lipid bilayer platform used to capture the CVB3 infectious virus by a focused, localized interaction with the receptor. In this approach, the nanodisc serves as a mock membrane, allowing the virus to bind asymmetrically to recapitulate the *in vivo* host cell binding event. The homogeneity and small diameter of nanodiscs are compatible with “single-particle” cryo-EM data collection and allow the nanodisc-virus complexes to adopt numerous orientations in the thin layer of vitrified ice. CAR-nanodiscs incubated at a 1:1 ratio with CVB3 at 4°C recruit virus capsid to the mock membrane without triggering A-particle formation (19, 20). CVB3-CAR-nanodisc complexes were then incubated for half an hour at 37°C, which has been shown to efficiently trigger A-particles without forcing global transformation of the capsid (19, 26, 34). Most of the nanodiscs remain associated with the A-particles after transition (fig. S1), with some particles clustering together, exhibiting hydrophobic characteristics of A-particles (21, 35).

Icosahedral symmetry averaging produces a 3.9 Å map

For the reconstructions of A-particle, images were collected automatically using EPU software on an FEI Tecnai Polara Microscope operating at 300 kV, equipped with an FEI Falcon II direct electron detector. Initially, 137,469 particles were selected from 9685 micrographs; however, about half of these particles had another A-particle located close by and were excluded from analysis. The remaining 62,327 particles were reconstructed in RELION (36) by imposing icosahedral symmetry to provide a high-resolution averaged map (Fig. 1), with the final resolution of 3.9 Å determined by where the Fourier shell correlation coefficient (FSC) fell below 0.143 (fig. S2, A and C). Separation of β strands and resolution of bulky side chains extending from the protein α backbone verify the resolution achieved, as seen in the sharpened map in Fig. 2 (A and C). The local resolution shows that the capsid shell has a resolution ranging from ~3.0 to 4.0, because

the inner surface and RNA genome are resolved at lower resolution as the genome is not icosahedrally ordered (fig. S3, A and B). Our CAR-nanodisc transitioned A-particle has undergone a slight expansion capsid-wide instead of the typical 4% expansion, and unlike globally stimulated A-particle structures, no holes were observed in the capsid shell either at the icosahedral twofold axis (11, 13, 18, 19) or at the quasi-threefold axis (Fig. 2B) (13).

Strong internal density corresponds to a retained RNA genome (Fig. 1B) that appears layered at high contour, as has been seen in other A-particles (Fig. 1C) (11). The connection between the viral proteins and RNA genome was weak, suggesting that the genome is remodeled at the capsid interface in preparation for escape. Retention of the genome immediately after A-particle formation is consistent with a physiologically accurate entry intermediate because RNA should remain encapsidated until its release is triggered ~30 to 90 min later (24–26), leaving behind an empty 80S capsid.

The new A-particle differs from the classical A-particle

A crystal structure of native CVB3 [Protein Data Bank (PDB) ID: 1COV] was used as a starting point to build the CAR-nanodisc A-particle structure (6). After fitting the structure into the map (37), the model was refined, with the icosahedral symmetry applied in real space using PHENIX, manually modified in Coot, and validated in MolProbity (38–40). The resulting protomer (Fig. 3A) was compared with the 1COV crystal structure by aligning the icosahedral symmetry axes to track movement during expansion to A-particle (Fig. 3B). The individual viral proteins were shifted outward by about 2.0 Å (table S1), with rigid body movements accounting for the expansion of the A-particle (13, 41). However, the residues comprising the inner surface of the capsid, such as VP4 and the N-terminal residues of VP1, VP2, and VP3, shifted less (0.8 to 1.2 Å) compared to other residues.

Unlike the globally stimulated A-particle of poliovirus, density for the pocket factor was evident, and most of the polypeptides of our CAR-nanodisc A-particle remained ordered, including VP4 and the N terminus of VP1. The residues for VP4 and the N terminus of VP1 shifted outward least among the viral polypeptides (Fig. 3B and table S1). However, contouring of the map suggested that the densities for VP4, internal VP1 N termini, and pocket factor in the CAR-nanodisc A-particle reconstruction were reduced in magnitude compared to other components of the capsid shell. This weaker density was verified with direct measurements that also identified the N-terminal

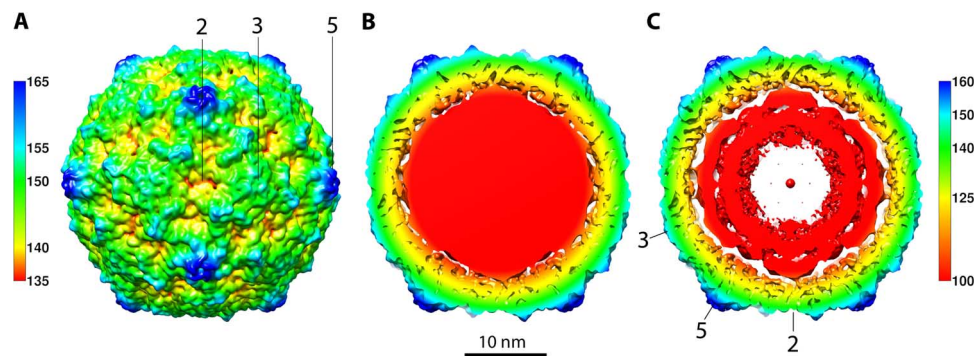


Fig. 1. Icosahedrally averaged A-particle formed asymmetrically. (A) The surface-rendered map of the CVB3 A-particle is colored radially according to the scale bar (numbers in Å), with the symmetry axes indicated. (B) The central section of the cryo-EM reconstruction shows strong density corresponding to the retained remodeled RNA genome (red). (C) Rendering the map at a higher contour (3σ above the mean) shows that the RNA genome is packed in layers inside the virus, as seen in CV-A16 (11).

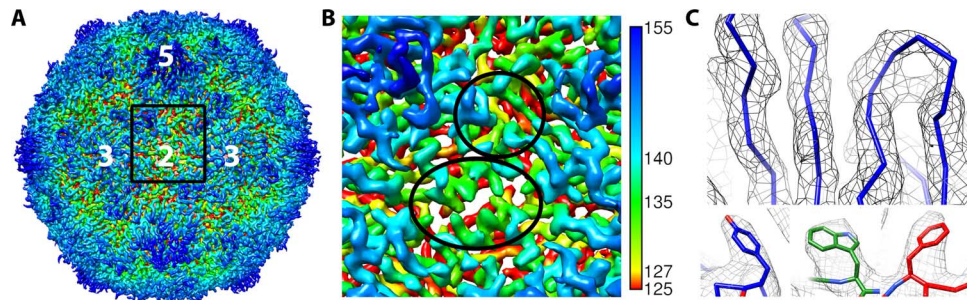


Fig. 2. Sharpened asymmetrically formed A-particle map. (A) The sharpened A-particle map is surface-rendered and radially colored according to the scale bar, with the icosahedral symmetry axes labeled. (B) The magnified square area shows no openings at the twofold axis and the quasi-threefold axis, as highlighted by the lower and upper black circles, respectively. (C) The quality of the map (gray mesh) is illustrated by the fit of the C α backbone in the separated β strands of the VP1 protein (blue wire), as well as the bulky side chains of Tyr¹¹⁵⁷, Trp²⁰⁷⁸, and Phe³²²⁰ (using the naming convention where residues in VP1, VP2, VP3, and VP4 are numbered sequentially, starting with 1001, 2001, 3001, and 4001, respectively).

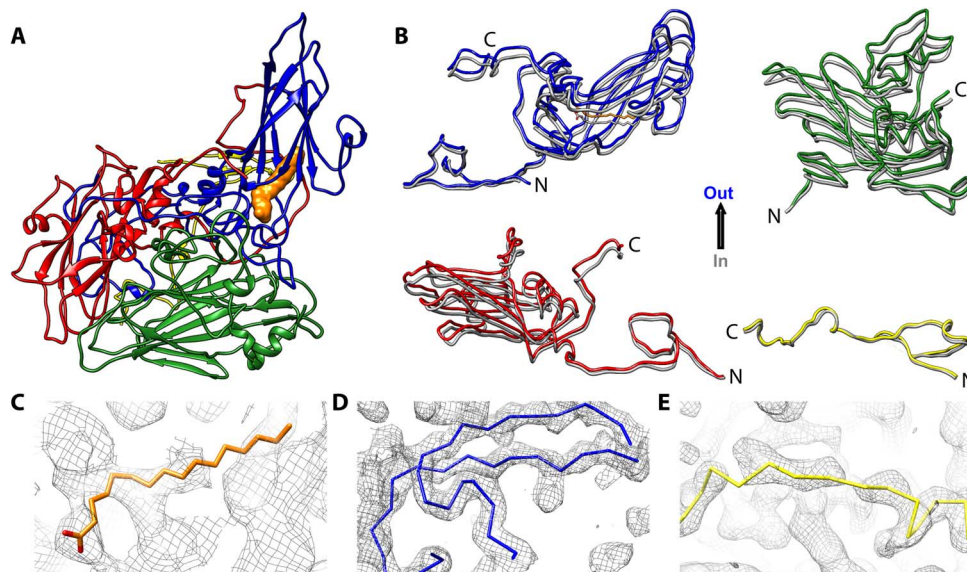


Fig. 3. Rigid body movements of virus proteins to form the CVB3 A-particle. (A) The structure of the CVB3 A-particle is shown as a ribbon diagram with VP1, VP2, VP3, and VP4 colored according to convention (blue, green, red, and yellow, respectively), with pocket factor rendered as an orange surface. (B) The four structural proteins of the A-particle (blue, green, red, and yellow) are aligned with the structure of CVB3 (dark gray) to illustrate the outward movements. (C to E) The structures of the pocket factor (orange wire), the N terminus of VP1 (blue wire), and the VP4 of CVB3 are shown fitted into the corresponding A-particle densities.

density of VP2 as significantly reduced in magnitude (fig. S5), suggesting that these sections of the structure are missing, flexible, or not incorporated into the capsid with icosahedral symmetry. A combination of these states is also possible. Therefore, using CAR-nanodisc to asymmetrically trigger A-particle formation does induce capsid expansion with rigid body movements.

A-particle is asymmetric

Using CAR-nanodisc to trigger A-particle formation is an asymmetric approach. Many studies have exploited icosahedral symmetry without imposing symmetry averaging to study the asymmetric features of viral structures (42–47). Briefly, in an approach sometimes termed “symmetry-mismatch reconstruction” (44), each particle is oriented first using symmetry operators, and then the icosahedral symmetry is released to a lower symmetry (C1) to identify those features that

do (and do not) follow icosahedral symmetry. To explore the asymmetry of the CAR-nanodisc A-particle, we used a symmetry release function (www.hafensteinlab.com/software.php) that we incorporated into our use of RELION (36). To avoid model bias during the asymmetric reconstructions, a low-pass filtered icosahedral map was used as the starting model. Initially, 1 of the 60 symmetry-related orientations was randomly assigned for each particle, and after several iterations, asymmetric features were identified in the map. The process continued until most of the particles did not change their orientations anymore and the map converged, resulting in a 7.8 Å resolution asymmetric map (Materials and Methods) (Fig. 4 and fig. S2, B and C).

The asymmetric 3D map did exhibit strong icosahedral symmetry except at the site of receptor engagement where relatively weak density is identified, distal from the capsid surface at the icosahedral threefold axis (Fig. 4A). This extra density is presumably a combination of

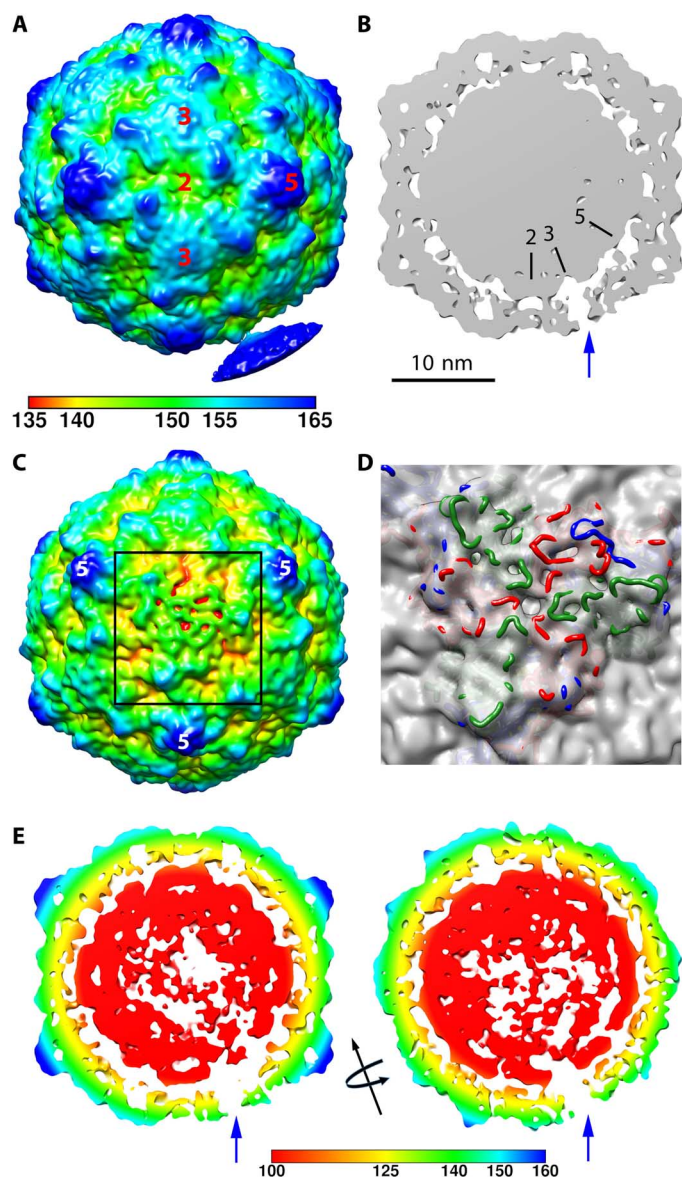


Fig. 4. Extending densities from the in situ CVB3 A-particle. (A) The asymmetric reconstruction is radially colored according to the key and surface-rendered at low contour to show the connection extruding from a single threefold to a nanodisc density. (B) A thin slice through the center of the map (gray density with symmetry axes marked) shows how the extruding density is visualized as a unique threefold pore (blue arrow) through the capsid shell at 2σ contour. (C) When the map with the same radial coloring as (A) is surface-rendered at 1.5σ , the unique site on the capsid adjacent to the nanodisc (black square outline) shows distinct weak density resulting from different protein extrusions becoming flexible upon extension. (D) The fitted capsid structure rendered in blue, red, and green wire for VP1, VP2, and VP3, respectively, shows how the protein loops extend through the weak capsid density at this asymmetric location only. (E) Left: A thin slice oriented the same as (B) but rendered at 2.75σ shows asymmetrically disordered genome densities. Right: The map was rotated 90° around the threefold axis (black arrow). Both slices are radially colored according to the key.

CAR-nanodiscs, flexible extruded viral proteins, and some residual neighboring particles left over after 3D classification. Noticeably, at low-contour level, densities extending from the capsid surface at the icosahedral threefold axis were observed (Fig. 4A). When shown at higher-contour levels, the rope-like extension extruding from the threefold appears to open into a pore (Fig. 4B), and the capsid surface degrades, forming channels (Fig. 4C). The thin slice of the reconstruction illustrates the hole at the threefold axis (Fig. 4B) and shows that the impaired capsid densities were accompanied by reduced interaction with the RNA genome. Additional analysis of the 3D map at higher-contour levels shows that the RNA genome asymmetrically changed the conformation. The RNA densities are directionally attenuated from the center toward the unique opening site (Fig. 4E), suggesting asymmetric reorganization of the genome for an exit. The rearrangement may be propagated from the site of receptor binding.

RNA-capsid interaction changes at the receptor engagement site

To identify RNA-capsid interactions, we placed the newly built asymmetric CVB3 A-particle structure into the 3.9 \AA icosahedrally averaged density map (Fig. 5). The N-terminal residues of VP1 were found to contribute the most to contacts with the RNA, especially at the icosahedral twofold and quasi-threefold (Fig. 5, fivefold close-ups) sites. In the asymmetric map, the remodeled surface area (adjacent to nanodisc) (Fig. 5C) was compared with the area at the opposite side of the capsid shell (Fig. 5B). Inspection shows that the RNA-capsid interactions at the site of receptor binding are attenuated at the threefold and fivefold sites, whereas the interaction beneath the twofold symmetry axis seems to be maintained. Specifically, at the site of receptor binding, asymmetric changes indicate a lost interaction with Tyr²⁰⁰⁹ and Gln⁴⁰⁰⁴ (using the naming convention where residues in VP1, VP2, VP3, and VP4 are numbered sequentially, starting with 1001, 2001, 3001, and 4001, respectively). The fact that Trp²⁰³⁸ is involved is notable because this highly conserved residue is located near the twofold axes, and its interaction with RNA has been noted before in rhinovirus and poliovirus (12, 48). Also, like the rhinovirus A-particle, Ser²⁰⁴⁵ interacts with the RNA at the twofold axis (12); however, we do not see any VP3-RNA interactions at the fivefold axis, probably because of the presence of VP4. The loss of contacts and density at the asymmetric threefold axis is unique.

Densities extend from the capsid surface

The newly built structure was superimposed onto the asymmetric cryo-EM map to characterize the local conformational change of the capsid; however, the electron densities of the opening area were too weak to be interpreted (Fig. 4, C and D). The local resolution of the map shows that the opening area of the capsid has a resolution significantly lower than the rest of the capsid (Fig. S4). This unique localized region of weak density and low resolution suggests that proteins around the opening have become flexible or exist in multiple conformations. Perhaps, as viral proteins exit the capsid, some fail to engage the lipid because of the small size of the nanodiscs. This would also explain why the nanodisc density is weak, because some discs are captured by one extruding virus protein and some are missed altogether. Resolving these densities at higher resolution can likely be addressed by using larger-diameter nanodiscs in a future study.

Using RELION 3D classification with our new symmetry-release function, we identified three different subclasses of A-particle structure

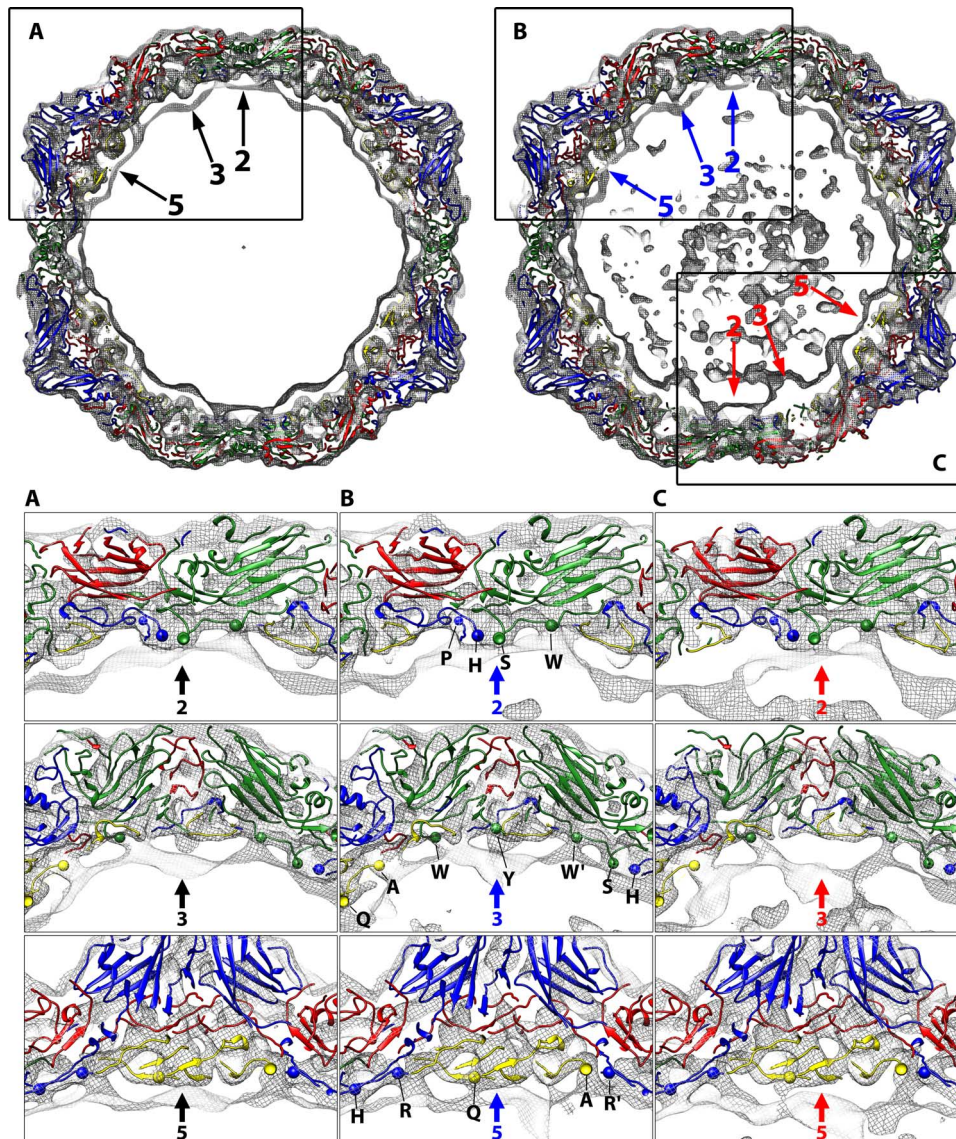


Fig. 5. Residues interacting with RNA genome. Top: Slabs (25 Å thick) of the icosahedral (left) and asymmetric (right) 3D maps viewed along an icosahedral twofold axis, with the newly built atomic model of the CAR-nanodisc A-particle. The viral proteins are colored accordingly, and the two-, three-, and fivefold icosahedral symmetric axes are indicated by arrows. (A to C) Subregions of the reconstructions (indicated in black rectangular outline) are shown in close-ups with the indicated symmetric axes. The asymmetric, remodeled region of the map (C) is distinguished by loss of density, especially notable in the threefold view. The slabs are parallel to but displaced ~15 Å closer (two- and fivefold) or farther (threefold) from the central section. Envelopes of protein shell and RNA density (gray mesh) are shown, with the virus structures fitted. Residues interacting with RNA are shown (spheres) from left to right and indicated with a one letter code in (B). The four residues in twofold close-ups are Pro¹⁰²², His¹⁰⁵², Ser²⁰⁴⁵, and Trp²⁰³⁸. The residues in threefold close-ups are Gln⁴⁰⁰⁴, Ala⁴⁰¹², Trp²⁰³⁸, [Tyr²⁰⁰⁹ only in (B)], Trp²⁰³⁸, Ser²⁰⁴⁵, and His¹⁰⁵². The five residues in fivefold close-ups are His¹⁰⁵², Arg¹⁰¹³, Gln⁴⁰⁰⁴, Ala⁴⁰¹², and Arg^{1013r}. The prime symbol (') indicates a symmetry-related residue.

that have extended tubes of density connected to putative nanodisc densities. These 3D maps were reconstructed to low resolution because of the small-particle counts but nonetheless show virus protein densities extending from either the threefold axis or the threefold propeller tip, or both (Fig. 6). Notably, this procedure did not identify any CAR density associated with the capsid, consistent with other A-particle expansions and loss of receptor binding site. The region near the propeller tip (Fig. 6A) is the known site for the N terminus of VP1 to be externalized for poliovirus, CV-A16, and rhino-

virus (11, 12, 23). This site of VP1 extension is consistent with A-particle. Moreover, in a picornavirus captured in the breathing state, VP1 extends also at the twofold axis, which is not seen here in our particle. This is the first time that the threefold axis (Fig. 6, B and C) has been identified as a site of extruding densities. The C terminus of VP4 and the N terminus of VP2 reside beneath the threefold axis (fig. S3C); however, it is unknown whether the extending densities at the threefold axis belong to VP4, other capsid proteins, or RNA.

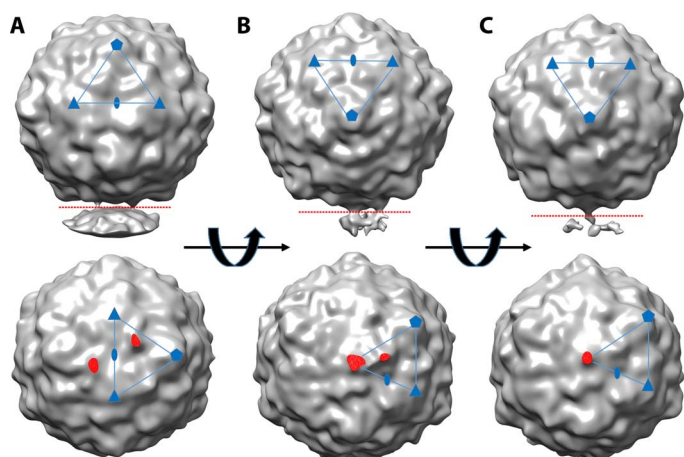


Fig. 6. Subclasses that have stronger threefold and propeller tip protein extensions can be classified. (A to C) Reconstructions surface-rendered in gray show the three maps from the subpopulations of asymmetric A-particles oriented to illustrate the densities. The upper panels show densities protruding downward away from the capsid, and the lower panels show each map that was cut where indicated (red dotted lines in the upper panels) and rotated 90°, with the protruding densities highlighted (red). The asymmetric units are indicated (blue lines and symbols). The subclasses consisted of (A) particles that have two density protrusions across the twofold at each propeller tip, (B) proteins exiting the threefold and the propeller tip, and (C) a strong rope-like density only at the threefold.

Protein densities reflect mobility at the site of receptor binding

The flexibility of the asymmetric proteins surrounding the opening led to the existence of multiple conformations and uninterpretable densities. Thus, instead of analyzing conformational changes of the proteins at the asymmetric opening, we measured the intensities of the electron density. Using both maps for comparison, the virus protein composition could be quantified (fig. S5). In the icosahedral reconstruction, VP4 showed lower intensity compared to other proteins, pocket factor had the lowest densities but was not absent, and the VP1 and VP2 N termini showed reduction in magnitude. The weaker presence of pocket factor supports a model where CAR interaction expelled the pocket factors locally and not capsid-wide.

For the asymmetric reconstruction, we compared the densities of the three protomers around the threefold axis to those of the other 57 protomers, demonstrating the impaired densities of VPs at the receptor-engaged area (Fig. 4D). All virus proteins and the pocket factor had weaker intensities in the unique pore area composed of the three protomers compared to the rest of the capsid. However, the intensities for VP4 change very little at the site of the opening compared to the capsid-wide VP4 intensity. The VP4 intensities in averaged and asymmetric reconstruction are also comparable, suggesting capsid-wide VP4 changes that are not limited to the asymmetric site. The weakness of the N-terminal residues of VP1 and VP2 in 57 protomers indicates that those residues are also flexible capsid-wide, perhaps because of the global capsid expansion and reordering of the RNA.

DISCUSSION

Improvements in hardware and software have led to an overall 7.8 Å asymmetric reconstruction of a 30-nm particle; however, we have

shown that the particle formed contained an asymmetric region corresponding to the three protomers on the capsid undergoing extensive remodeling, including the extrusion of proteins and subsequent disorder. Thus, it is technically important to note that the icosahedrally averaged map of these asymmetric particles attained a 3.9 Å resolution. Attaining this high resolution upon averaging distinctly asymmetric features into the capsid map illustrates what can be missed in other cases by imposing icosahedral averaging.

Previously solved A-particle maps differ in capsid composition and conformation compared to the asymmetrically triggered A-particle map presented here. Specifically, other structures show the capsid-wide externalization of the VP1 N termini, complete loss of VP4 (11, 13, 18, 19), and exit of all pocket factor (20) accompanied by an irreversible 4% expansion of the capsids, leading to the holes at the icosahedral twofold axis. This classical A-particle has been considered the entry intermediate, although all the high-resolution structures were triggered by global stimulation of capsids upon application of excess receptors or other external stimuli. However, here, we have triggered capsids with a local, focused application of a full-length receptor embedded in a lipid bilayer nanodisc. This approach, using a mock membrane to present a receptor to a virus, provides a targeted stimulus that transitions the capsid to an asymmetric entry intermediate with both global and local changes. Our findings are not consistent with a particle captured in a breathing state, because this particle lacks VP1 extrusions at the twofold axis and is only slightly expanded (12, 49). This first high-resolution view of an asymmetric receptor-stimulated particle is 2% radially expanded and has partial loss of pocket factor and alterations to viral proteins, especially at the site of receptor engagement. Although the capsids underwent marked structural rearrangement, the genome is retained, suggesting that this particle is physiologically on-pathway (25). The locally stimulated A-particle may be an early intermediate that will have to change further to become like the classical A-particle. Alternatively, the structure may represent a more accurate physiological entry intermediate due to the local stimulation by the receptor. Nevertheless, this novel finding suggests that binding of receptor drives the conformational rearrangement at a unique capsid site to initiate the eventual genome release during entry.

We propose a model whereby receptor interaction triggers the first change in the capsid as the release of those copies of pocket factor nearest the site of receptor interaction. The egress of pocket factor is followed by the VP1 N termini exiting the capsid to anchor the particle at the membrane. Capsid expansion may occur during or immediately after VP1 tethering, which would prevent the A-particle from losing contact with the membrane, because expansion is accompanied by loss of CAR binding. A capsid-wide movement of the N termini of the capsid proteins VP1 and VP2 at the interior suggests that expansion is accompanied by internal conformational changes designed to set up release of the genome. It is likely that the N terminus of VP3 moves less because it is trapped between the VP1 and VP4 at the fivefold. Movement of VP4 occurs capsid-wide, with VP4 escaping the capsid near the receptor binding site, allowing for VP4 membrane insertion and pore formation (Fig. 7).

The use of nanodiscs and the recent advances in cryo-EM technology have allowed this first glimpse of asymmetric capsid changes and their function during entry, which is critical to understanding the exact structural rearrangements that occur in preparation for genome release. The small-diameter nanodisc (10 nm) has been fruitful in revealing local dynamics in capsid structures that are not captured with

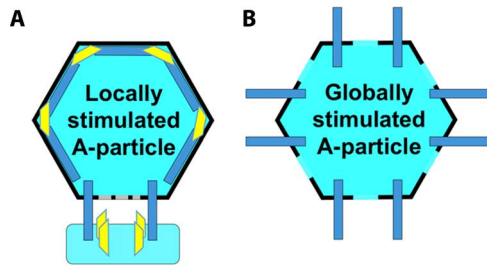


Fig. 7. Two A-particles resulting from different stimulations. (A and B) Schematic representation of the locally stimulated (A) and globally stimulated A-particle (B). Locally stimulated A-particle has pores only at the site of receptor engagement and asymmetrically externalizes the VP4s and the VP1 N termini around the receptor binding site, whereas the globally stimulated A-particle has global twofold openings and externalizes all VP4s and the VP1 N termini.

global stimulation while only minimally interfering with capsid images that are coprojected with it. What remains to be revealed is the next step that triggers the transfer of the RNA genome into the host cell, as well as whether this step is dependent on the asymmetric arrangement of the packaged genome relative to the unique capsid site selected by receptor interaction. Understanding these changes in detail will allow for the directed design of antivirals, allowing for greater treatment options for many viral infections.

MATERIALS AND METHODS

Knob column production

Escherichia coli BL21 cells transfected with an adenovirus 12 His-tagged knob expression vector were grown in an LB medium, as previously described (50). The protein was pelleted by centrifugation at 10,000 rpm for 5 min at 4°C. The pellet was resuspended in binding buffer [20 mM sodium phosphate (pH 7.4), 30 mM imidazole, and 500 mM NaCl], and the knob was purified using a 5-ml HisTrap column on the GE ÄKTA. Fractions containing the protein were pooled and dialyzed overnight at 4°C into 0.1 M NaHCO₃ and 0.5 M NaCl (pH 8.5). The purified knob (0.88 mg) was added to 10 ml of cold 0.1 M NaHCO₃ and 0.5 M NaCl (pH 8.5). Affi-Gel 10 beads were prepared according to the manufacturer's instructions and placed in a disposable column. The cold knob solution was added to the beads, and the slurry was allowed to mix with gentle agitation overnight at 4°C.

CAR expression and purification

A9-CAR cells (clone 2498.5) stably expressing the human CAR protein were grown at 37°C to confluence. Cells were harvested by scraping after washing with 10 ml of CAR purification buffer [20 mM tris (pH 7.6), 150 mM NaCl, and 5 mM EDTA] supplemented with phenylmethylsulfonyl fluoride. Cells were pelleted by centrifugation at 1000g for 5 min at 4°C and resuspended in 50 ml of CAR purification buffer supplemented with 2% octyl glucoside (OG). After 5 min of incubation on ice, the cells were vigorously vortexed and centrifuged at 4500 rpm for 15 min at 4°C to pellet cell nuclei and debris. The supernatant was harvested and stored at -80°C until purification. The knob affinity column was conditioned by washing with running buffer [20 mM tris (pH 7.6) and 150 mM NaCl], 10% acetic acid with 2% OG, and running buffer supplemented with 2% OG. A9-CAR lysate (15 ml) was applied to the column; flow-through was collected and reapplied

to the column. The column was washed with running buffer, and CAR was eluted with 10% acetic acid with 2% OG into ten 200- μ l fractions. Optical density readings at a wavelength of 280 nm were collected for each fraction, and fractions with readings greater than 0.1 were pooled and dialyzed into 20 mM tris (pH 7.5), 150 mM NaCl, and 1% OG overnight at 4°C.

Nanodisc formation

E. coli BL21 cells transfected with His-tagged MSP1E1 expression vector were grown and lysed, and supernatants were collected as previously described (51). The resulting supernatants were used for MSP1E1 purification using a 5-ml HisTrap column on the GE ÄKTA. Fractions containing protein were pooled and dialyzed overnight at 4°C into 10 mM tris (pH 7.4), 100 mM NaCl, and 1 mM EDTA. Aponeanodiscs were formed from MSP1E1 and DPPC (dipalmitoylphosphatidylcholine) lipids as previously described (51). CAR-nanodiscs were formed using a calculated ratio of 0.5 CAR molecules per nanodisc in an MSP1E1/CAR/DPPC ratio of 0.92:0.42:1.34. Components were incubated in a glass vial with a Teflon lid at 37°C for 90 min after gentle mixing. The mixture was transferred to a dialysis cassette with a molecular weight cutoff of 3.5 kD. The dialysis reaction was allowed to proceed for 24 hours with four buffer changes at 37°C to remove the detergent and, thus, allow lipid bilayers to form, constrained by the MSP1E1 proteins acting as a scaffold to shape the nanodisc formation.

Cryo-EM data collection

CVB3 was propagated and purified as previously described (19). Complexes were made by incubating 5 μ l of formed CAR-nanodiscs with 20 μ l of CVB3 (1 mg/ml) on ice for 1 hour. Grids imaged in a JEOL 2100 microscope were blotted and vitrified in liquid ethane using a Gatan Cryoplunge 3 plunge robot. The sample was applied to a glow-discharged, continuous carbon film-supported QUANTIFOIL EM grid. The microscope was operated at an accelerating voltage of 200 kV using a nominal magnification of $\times 50,000$, resulting in a calibrated pixel size of 2.33 Å.

CVB3 was transitioned to A-particle by raising the temperature to 37°C for 30 min. Grids were imaged in a Polara microscope using the FEI EPU software. An "atlas" image was assembled from micrographs taken at $\times 58$ magnification on a Gatan Orius CCD (charge-coupled device) camera, and suitable areas were selected for imaging on a Falcon II direct electron detector. The microscope was operated at 300 kV, with no objective aperture and with a 70- μ m condenser aperture. The beam was condensed to allow four nonoverlapping exposures per 2- μ m-diameter hole in a QUANTIFOIL R2/2 mesh, despite the consequent departure from parallel illumination. The nominal magnification of $\times 78,000$ and post-column magnification of $\times 1.4$ yielded calibrated pixels of 1.37 Å at the sample. Total dose per exposure was estimated at 30 e⁻/Å².

Initial icosahedral and asymmetric reconstruction

Individual particles (137,469) were selected, linearized, and normalized using an X3D software program (52). The contrast transfer function of each micrograph was estimated using CTFFIND4 (53). Upon examination of the raw data, many capsids were found to be clustered with neighboring particles, suggesting that some capsids had bound to more than one CAR-nanodisc or that the hydrophobic nature of the A-particle caused clumping. Using Auto3DEM (54), we

generated an initial icosahedral model and added a volume of cylindrical density, which was filtered to a resolution of 40 Å and used to generate a model with the “*icos_equiv*” option (54). This output map was used to sort the particles in an initial 3D classification by RELION (36). Before the 3D classification without symmetry (C1), particle images were reextracted from micrographs, and reference-free 2D classification was done to remove bad particles. Three of the resulting four 3D classes (classes 1 to 3) contained 75,142 particles, which have multiple adjacent particles, whereas the fourth class (class 4) contained 62,327 particles mostly without adjacent particles. Further analysis confirmed that classes 1 to 3 have multiple weakened areas of the capsid shell, suggesting that the virus particles were engaged with multiple receptors and that the fourth class have one weak area probably engaged with one or two receptors. Because our research focus was to study the locally stimulated A-particle, hereafter, we only used the class 4 particles for further analysis, although the first three classes also produced similar results.

Icosahedral reconstruction and model building

The icosahedral reconstruction with particles in the selected class 4 was completed using icosahedral symmetry operators in RELION (36). A total of 5124 particles in class 4 were discarded (described below), and 57,203 particles were used for the final icosahedral reconstruction (table S2). The FSC curve fell below 0.143 at a resolution of 3.9 Å. The resulting electron density map was sharpened using EMBACTOR (55) by applying a B factor of -193 \AA^2 .

Building of the model into the sharpened map was initiated by fitting the CVB3 crystal structure (PDB ID: 1COV) (5) as a rigid body in Chimera (6). The fitted structure of an asymmetric unit was duplicated for 60 icosahedral units and refined with noncrystallographic symmetry using PHENIX real space refine (38, 40). The map cross-correlation values for “whole unit cell” and “around atoms” were 0.748 and 0.832, respectively. The root mean square deviation values for bonds and angles were 0.01 and 0.74, respectively. The Ramachandran outlier was 0.12%. The refined model was visually inspected and modified in Coot (39) and validated by MolProbity (56).

Asymmetric reconstruction with iterative symmetric relaxation alignment

Instead of using a python script as in Zhang *et al.* (45), we modified the RELION C++ source code to incorporate an additional function, “*sym_break*,” that restricts the searching orientations of the expectation step to the 60 views related by icosahedral symmetry (or any kinds of symmetry operators in RELION), same as the “*icos_equiv*” option in AUTO3DEM (54) or “*symmetry relaxation method*” in j3dr (42). The *sym_break* refinement was used in the 3D classification run type using single or multiple classes. The predetermined orientation and center parameters for each particle from the icosahedral refinement were used as inputs, and only orientations were allowed to change during iterations. The icosahedral 3D map was low-pass filtered and used as an initial model to avoid model bias. To select a single orientation among the 60 views, we used a cross-correlation method instead of maximum likelihood in RELION. Asymmetric features emerged from the random assignment after one to two iterations. To slow the progression of the refinement, we used a T factor of 0.5 in RELION. The change in orientation of each particle was monitored to check the progress. Once the resolution of the model did not improve and less than 0.05% of the particles changed their orientations, the resulting model

was then low-pass filtered again and used as an initial model for the next round of refinement. Several rounds of this process were done to prevent trapping into local minima in the orientation assignment (45). The process was repeated until the model converged. To ensure that the correct asymmetric reconstruction was obtained, the whole routine of iterative steps was repeated multiple times to obtain consistent asymmetric structures. After the refinement with *sym_break*, local refinement with C1 symmetry was performed in RELION, resulting in the 7.8 Å reconstruction based on an FSC threshold of 0.5 (fig. S2, B and C). The 3D map was sharpened using EMBACTOR (55) by applying a B factor of -397 \AA^2 .

To investigate whether distinct classes of structures might be present in the selected class 4 particles (table S2), we performed 3D classifications with the *sym_break* option as previously described, but using five to six class members to examine heterogeneity of the particles used. This approach found three classes that revealed extending densities from the capsid surface but each with a small number of particles (Fig. 5). It also found another 3D class for which the capsid structure seemed relatively intact. This class might include particles that had not engaged with the receptors; therefore, the icosahedral and asymmetric reconstructions were repeated after excluding the particles. The final reported reconstructions include 57,208 particles (table S2).

Structural display and analysis

Map visualization and images were generated in Chimera (37) and Bshow (57). Local resolution estimates were completed using ResMap (58). Quantifying the magnitude of densities corresponding to VP1 to VP4, N-terminal VP1 to VP3, and pocket factor was done in Chimera (37). To measure the mean values of these structural entities (table S1), masks generated by the “*molmap*” function in Chimera from the corresponding atomic models for each structure were applied to the unfiltered icosahedral and asymmetric maps. To get the density intensity corresponding to each part, the mean values were multiplied by the map dimension and divided by the volume of each mask. Finally, the results were compensated for the background mean intensity of each map and normalized for the mean of VP1 protein in each map.

SUPPLEMENTARY MATERIALS

Supplementary material for this article is available at <http://advances.sciencemag.org/cgi/content/full/2/8/e1501929/DC1>

fig. S1. Negative-stain transmission electron microscopy images of CAR-nanodiscs bound to CVB3.

fig. S2. Central sections and FSC curves of the icosahedral and asymmetric 3D maps.

fig. S3. Local resolution of the icosahedral 3D reconstruction.

fig. S4. Local resolution of the asymmetric 3D reconstruction.

fig. S5. Quantification of density.

table S1. Superimposing CVB3 (PDB ID: 1COV) with CAR-nanodisc A-particle structure illustrates rigid body movement of the protomer and describes the expansion of about 2 Å.

table S2. Classification of the CAR-nanodisc particles.

REFERENCES AND NOTES

- Centers for Disease Control and Prevention, Nonpolio enterovirus and human parvovirus surveillance—United States, 2006–2008. *MMWR Morb. Mortal. Wkly. Rep.* **59**, 1577–1580 (2010).
- K.-S. Kim, G. Hufnagel, N. M. Chapman, S. Tracy, The group B coxsackieviruses and myocarditis. *Rev. Med. Virol.* **11**, 355–368 (2001).
- P. E. Tam, Coxsackievirus myocarditis: Interplay between virus and host in the pathogenesis of heart disease. *Viral Immunol.* **19**, 133–146 (2006).

4. S. Tracy, K. M. Drescher, N. M. Chapman, K.-S. Kim, S. D. Carson, S. Pirruccello, P. H. Lane, J. R. Romero, J. S. Leser, Toward testing the hypothesis that group B coxsackieviruses (CVB) trigger insulin-dependent diabetes: Inoculating nonobese diabetic mice with CVB markedly lowers diabetes incidence. *J. Virol.* **76**, 12097–12111 (2002).
5. S. Tracy, K. Höfling, S. Pirruccello, P. H. Lane, S. M. Reyna, C. J. Gauntt, Group B coxsackievirus myocarditis and pancreatitis: Connection between viral virulence phenotypes in mice. *J. Med. Virol.* **62**, 70–81 (2000).
6. J. K. Muckelbauer, M. Kremer, I. Minor, G. Diana, F. J. Dutko, J. Groarke, D. C. Pevear, M. G. Rossmann, The structure of coxsackievirus B3 at 3.5 Å resolution. *Structure* **3**, 653–667 (1995).
7. J. M. Bergelson, J. A. Cunningham, G. Droguett, E. A. Kurt-Jones, A. Krithivas, J. S. Hong, M. S. Horwitz, R. L. Crowell, R. W. Finberg, Isolation of a common receptor for coxsackie B viruses and adenoviruses 2 and 5. *Science* **275**, 1320–1323 (1997).
8. N. Guttman, D. Baltimore, A plasma membrane component able to bind and alter virions of poliovirus type 1: Studies on cell-free alteration using a simplified assay. *Virology* **82**, 25–36 (1977).
9. Y. He, P. R. Chipman, J. Howitt, C. M. Bator, M. A. Whitt, T. S. Baker, R. J. Kuhn, C. W. Anderson, P. Freimuth, M. G. Rossmann, Interaction of coxsackievirus B3 with the full length coxsackievirus-adenovirus receptor. *Nat. Struct. Biol.* **8**, 874–878 (2001).
10. M. G. Rossmann, Viral cell recognition and entry. *Protein Sci.* **3**, 1712–1725 (1994).
11. J. Ren, X. Wang, Z. Hu, Q. Gao, Y. Sun, X. Li, C. Porta, T. S. Walter, R. J. Gilbert, Y. Zhao, D. Axford, M. Williams, K. McAuley, D. J. Rowlands, W. Yin, J. Wang, D. I. Stuart, Z. Rao, E. E. Fry, Picornavirus uncoating intermediate captured in atomic detail. *Nat. Commun.* **4**, 1929 (2013).
12. A. Pickl-Herk, D. Luque, L. Vives-Adrián, J. Querol-Audí, D. Garriga, B. L. Trus, N. Verdaguer, D. Blaas, J. R. Castón, Uncoating of common cold virus is preceded by RNA switching as determined by x-ray and cryo-EM analyses of the subviral A-particle. *Proc. Natl. Acad. Sci. U.S.A.* **110**, 20063–20068 (2013).
13. C. Butan, D. J. Filman, J. M. Hogle, Cryo-electron microscopy reconstruction shows poliovirus 135S particles poised for membrane interaction and RNA release. *J. Virol.* **88**, 1758–1770 (2014).
14. D. Bebeck, D. J. Filman, J. M. Hogle, Cryo-electron microscopy reconstruction of a poliovirus receptor-membrane complex. *Nat. Struct. Mol. Biol.* **12**, 615–618 (2005).
15. M. Bostina, H. Levy, D. J. Filman, J. M. Hogle, Poliovirus RNA is released from the capsid near a twofold symmetry axis. *J. Virol.* **85**, 776–783 (2011).
16. M. Strauss, H. C. Levy, M. Bostina, D. J. Filman, J. M. Hogle, RNA transfer from poliovirus 135S particles across membranes is mediated by long umbilical connectors. *J. Virol.* **87**, 3903–3914 (2013).
17. M. Kumar, D. Blaas, Human rhinovirus subviral a particle binds to lipid membranes over a twofold axis of icosahedral symmetry. *J. Virol.* **87**, 11309–11312 (2013).
18. K. L. Shingler, J. L. Yoder, M. S. Carnegie, R. E. Ashley, A. M. Makhov, J. F. Conway, S. Hafenstein, The enterovirus 71 A-particle forms a gateway to allow genome release: A cryoEM study of picornavirus uncoating. *PLOS Pathog.* **9**, e1003240 (2013).
19. L. J. Organtini, A. M. Makhov, J. F. Conway, S. Hafenstein, S. D. Carson, Kinetic and structural analysis of coxsackievirus B3 receptor interactions and formation of the A-particle. *J. Virol.* **88**, 5755–5765 (2014).
20. M. Strauss, D. J. Filman, D. M. Belnap, N. Cheng, R. T. Noel, J. M. Hogle, Nectin-like interactions between poliovirus and its receptor trigger conformational changes associated with cell entry. *J. Virol.* **89**, 4143–4157 (2015).
21. C. E. Fricks, J. M. Hogle, Cell-induced conformational change in poliovirus: Externalization of the amino terminus of VP1 is responsible for liposome binding. *J. Virol.* **64**, 1934–1945 (1990).
22. A. Panjwani, M. Strauss, S. Gold, H. Wenham, T. Jackson, J. J. Chou, D. J. Rowlands, N. J. Stonehouse, J. M. Hogle, T. J. Tuthill, Capsid protein VP4 of human rhinovirus induces membrane permeability by the formation of a size-selective multimeric pore. *PLOS Pathog.* **10**, e1004294 (2014).
23. J. Lin, N. Cheng, M. Chow, D. J. Filman, A. C. Steven, J. M. Hogle, D. M. Belnap, An externalized polypeptide partitions between two distinct sites on genome-released poliovirus particles. *J. Virol.* **85**, 9974–9983 (2011).
24. B. Brandenburg, L. Y. Lee, M. Lakadamyali, M. J. Rust, X. Zhuang, J. M. Hogle, Imaging poliovirus entry in live cells. *PLOS Biol.* **5**, e183 (2007).
25. C. B. Coyne, J. M. Bergelson, Virus-induced Abl and Fyn kinase signals permit coxsackievirus entry through epithelial tight junctions. *Cell* **124**, 119–131 (2006).
26. J. M. Bergelson, C. B. Coyne, in *Viral Entry into Host Cells*, S. Pöhlmann, G. Simmons, Eds. (Springer Science, New York, NY, 2013), vol. 790, pp. 24–41.
27. M. G. Campbell, D. Veessler, A. Cheng, C. S. Potter, B. Carragher, 2.8 Å resolution reconstruction of the *Thermoplasma acidophilum* 20S proteasome using cryo-electron microscopy. *ELife* **4**, e06380 (2015).
28. A. Bartesaghi, D. Matthies, S. Banerjee, A. Merk, S. Subramaniam, Structure of β-galactosidase at 3.2-Å resolution obtained by cryo-electron microscopy. *Proc. Natl. Acad. Sci. U.S.A.* **111**, 11709–11714 (2014).
29. V. A. M. Gold, R. Salzer, B. Averhoff, W. Kühlbrandt, Structure of a type IV pilus machinery in the open and closed state. *ELife* **4**, e07380 (2015).
30. W. Kühlbrandt, The resolution revolution. *Science* **343**, 1443–1444 (2014).
31. N. Shirzad-Wasei, J. van Oostrum, P. H. M. Bovee-Geurts, L. J. A. Kusters, G. J. C. G. M. Bosman, W. J. DeGrip, Rapid transfer of overexpressed integral membrane protein from the host membrane into soluble lipid nanodiscs without previous purification. *Biol. Chem.* **396**, 903–915 (2015).
32. Y. Yao, L. M. Fujimoto, N. Hirshman, A. A. Bobkov, A. Antignani, R. J. Youle, F. M. Marassi, Conformation of BCL-XL upon membrane integration. *J. Mol. Biol.* **427**, 2262–2270 (2015).
33. W.-S. Choi, W. J. Rice, D. L. Stokes, B. S. Collier, Three-dimensional reconstruction of intact human integrin αIIbβ3: New implications for activation-dependent ligand binding. *Blood* **122**, 4165–4171 (2013).
34. A. M. Milstone, J. Petrella, M. D. Sanchez, M. Mahmud, J. C. Whitbeck, J. M. Bergelson, Interaction with coxsackievirus and adenovirus receptor, but not with decay-accelerating factor (DAF), induces A-particle formation in a DAF-binding coxsackievirus B3 isolate. *J. Virol.* **79**, 655–660 (2005).
35. N. Guttman, D. Baltimore, Morphogenesis of poliovirus. IV. Existence of particles sedimenting at 150S and having the properties of provirion. *J. Virol.* **23**, 363–367 (1977).
36. S. H. W. Scheres, RELION: Implementation of a Bayesian approach to cryo-EM structure determination. *J. Struct. Biol.* **180**, 519–530 (2012).
37. E. F. Pettersen, T. D. Goddard, C. C. Huang, G. S. Couch, D. M. Greenblatt, E. C. Meng, T. E. Ferrin, UCSF Chimera—A visualization system for exploratory research and analysis. *J. Comput. Chem.* **25**, 1605–1612 (2004).
38. P. D. Adams, P. V. Afonine, G. Bunkóczi, V. B. Chen, I. W. Davis, N. Echols, J. J. Headd, L.-W. Hung, G. J. Kapral, R. W. Grosse-Kunstleve, A. J. McCoy, N. W. Moriarty, R. Oeffner, R. J. Read, D. C. Richardson, J. S. Richardson, T. C. Terwilliger, P. H. Zwart, PHENIX: A comprehensive Python-based system for macromolecular structure solution. *Acta Crystallogr. Sect. D Biol. Crystallogr.* **66**, 213–221 (2010).
39. P. Emsley, B. Lohkamp, W. G. Scott, K. Cowtan, Features and development of Coot. *Acta Crystallogr. Sect. D Biol. Crystallogr.* **66**, 486–501 (2010).
40. P. V. Afonine, J. J. Headd, T. C. Terwilliger, P. D. Adams, New Tool: phenix.real_space_refine. *Comput. Crystallography Newsl.* **4**, 43–44 (2013).
41. X. Wang, W. Peng, J. Ren, Z. Hu, J. Xu, Z. Lou, X. Li, W. Yin, X. Shen, C. Porta, T. S. Walter, G. Evans, D. Axford, R. Owen, D. J. Rowlands, J. Wang, D. I. Stuart, E. E. Fry, Z. Rao, A sensor-adaptor mechanism for enterovirus uncoating from structures of EV71. *Nat. Struct. Mol. Biol.* **19**, 424–429 (2012).
42. W. Jiang, J. Chang, J. Jakana, P. Weigele, J. King, W. Chiu, Structure of epsilon15 bacteriophage reveals genome organization and DNA packaging/injection apparatus. *Nature* **439**, 612–616 (2006).
43. F. Guo, Z. Liu, F. Vago, Y. Ren, W. Wu, E. T. Wright, P. Serwer, W. Jiang, Visualization of uncorrelated, tandem symmetry mismatches in the internal genome packaging apparatus of bacteriophage T7. *Proc. Natl. Acad. Sci. U.S.A.* **110**, 6811–6816 (2013).
44. H. Liu, L. Cheng, Cryo-EM shows the polymerase structures and a nonspooled genome within a dsRNA virus. *Science* **349**, 1347–1350 (2015).
45. X. Zhang, K. Ding, X. Yu, W. Chang, J. Sun, Z. H. Zhou, In situ structures of the segmented genome and RNA polymerase complex inside a dsRNA virus. *Nature* **527**, 531–534 (2015).
46. S. Hafenstein, L. M. Palermo, V. A. Kostyuchenko, C. Xiao, M. C. Morais, C. D. S. Nelson, V. D. Bowman, A. J. Battisti, P. R. Chipman, C. R. Parrish, M. G. Rossmann, Asymmetric binding of transferrin receptor to parvovirus capsids. *Proc. Natl. Acad. Sci. U.S.A.* **104**, 6585–6589 (2007).
47. H. Lee, J. O. Cifuentes, R. E. Ashley, J. F. Conway, A. M. Makhov, Y. Tano, H. Shimizu, Y. Nishimura, S. Hafenstein, A strain-specific epitope of enterovirus 71 identified by cryo-electron microscopy of the complex with Fab from neutralizing antibody. *J. Virol.* **87**, 11363–11370 (2013).
48. H. C. Levy, M. Bostina, D. J. Filman, J. M. Hogle, Catching a virus in the act of RNA release: A novel poliovirus uncoating intermediate characterized by cryo-electron microscopy. *J. Virol.* **84**, 4426–4441 (2010).
49. J. Lin, L. Y. Lee, M. Roivainen, D. J. Filman, J. M. Hogle, D. M. Belnap, Structure of the Fab-labeled “breathing” state of native poliovirus. *J. Virol.* **86**, 5959–5962 (2012).
50. P. Freimuth, K. Springer, C. Berard, J. Hainfeld, M. Bewley, J. Flanagan, Coxsackievirus and adenovirus receptor amino-terminal immunoglobulin V-related domain binds adenovirus type 2 and fiber knob from adenovirus type 12. *J. Virol.* **73**, 1392–1398 (1999).
51. I. G. Denisov, Y. V. Grinkova, A. A. Lazarides, S. G. Sligar, Directed self-assembly of mono-disperse phospholipid bilayer nanodiscs with controlled size. *J. Am. Chem. Soc.* **126**, 3477–3487 (2004).
52. J. F. Conway, A. C. Steven, Methods for reconstructing density maps of “single” particles from cryoelectron micrographs to subnanometer resolution. *J. Struct. Biol.* **128**, 106–118 (1999).
53. A. Rohou, N. Grigorieff, CTFFIND4: Fast and accurate defocus estimation from electron micrographs. *J. Struct. Biol.* **192**, 216–221 (2015).
54. X. Yan, R. S. Sinkovits, T. S. Baker, AUTO3DEM—An automated and high throughput program for image reconstruction of icosahedral particles. *J. Struct. Biol.* **157**, 73–82 (2007).

55. J. J. Fernández, D. Luque, J. R. Castón, J. L. Carrascosa, Sharpening high resolution information in single particle electron cryomicroscopy. *J. Struct. Biol.* **164**, 170–175 (2008).
56. V. B. Chen, W. B. Arendall III, J. J. Headd, D. A. Keedy, R. M. Immormino, G. J. Kapral, L. W. Murray, J. S. Richardson, D. C. Richardson, MolProbity: All-atom structure validation for macromolecular crystallography. *Acta Crystallogr. Sect. D Biol. Crystallogr.* **D66**, 12–21 (2010).
57. J. B. Heymann, Bsoft: Image and molecular processing in electron microscopy. *J. Struct. Biol.* **133**, 156–169 (2001).
58. A. Kucukelbir, F. J. Sigworth, H. D. Tagare, Quantifying the local resolution of cryo-EM density maps. *Nat. Methods* **11**, 63–65 (2013).

Acknowledgments: We thank P. Tattersall and S. Cotmore of Yale and P. Freimuth of Brookhaven for providing the CAR expression cells. **Funding:** This work was supported in part by the Pennsylvania Department of Health CURE (Commonwealth Universal Research Enhancement Program) funds. This study was also supported by the Office of the Director, NIH, under award nos. S10OD019995 (to J.F.C.) and S10OD011986 (to S.H.), as well as NIH grants R01AI107121 (to S.H.) and T32CA060395 (to K.L.S.). The content is solely the responsibility of the authors and does not necessarily represent the official views of the NIH. **Author contributions:** H.L. contributed to the experimental design and did all reconstructions, map interpretation, and model

building; K.L.S. prepared virus, nanodisc, and CAR samples; L.J.O. propagated and purified virus; R.E.A. provided negative stain TEM; A.M.M. and J.F.C. performed cryo-EM; and S.H. contributed experimental design, data analysis, and map interpretation. The manuscript was written by H.L., K.L.S., J.F.C., and S.H. **Competing interests:** The authors declare that they have no competing interests. **Data and materials availability:** All data needed to evaluate the conclusions in the paper are present in the paper and/or the Supplementary Materials. Additional data related to this paper may be requested from the authors. The cryo-EM density maps and atomic coordinates for the CVB3 locally stimulated A-particle are available at the Electron Microscopy Data Bank and PDB via accession codes EMD-6636 (unsharpened icosahedral map), EMD-6637 (sharpened icosahedral map), EMD-6638 (asymmetric map), and J3D7.

Submitted 30 December 2015

Accepted 28 July 2016

Published 24 August 2016

10.1126/sciadv.1501929

Citation: H. Lee, K. L. Shingler, L. J. Organtini, R. E. Ashley, A. M. Makhov, J. F. Conway, S. Hafenstein, The novel asymmetric entry intermediate of a picornavirus captured with nanodiscs. *Sci. Adv.* **2**, e1501929 (2016).